CHAPTER 5

Combined Effect of Cyclic Loading, Impeded Boundary Conditions and Non- Darcian Flow on Saturated Consolidation

5.1 INTRODUCTION

In the previous chapters, consolidation analyses were carried out through uncoupled methods where it is assumed that the dissipation of excess pore water pressure (u) and the deformation (s) of the soil skeleton are considered to be mutually exclusive. Although, uncoupled methods may oversimplify the consolidation process, but in heterogeneous soil profiles, when dealing with soil layers of varying permeability and time-dependent loading conditions, it leads to inaccuracies in settlement predictions. On the contrary, the coupled methods had the mutual influence of pore water pressure dissipation and soil deformation, which provided a more comprehensive and precise representation of the consolidation process. Biot (1941) introduced a comprehensive theory for three-dimensional consolidation, which incorporates the coupling between soil deformation and pore pressure. He showed that the total stress may change during the consolidation as opposed to the constant total stress considered by Terzaghi and Rendulic (1936) for the 3-D uncoupled consolidation theory. The solutions of these two theories are different from each other. For uncoupled consolidation, the initial excess pore water pressure, which is equal to the magnitude of the applied load, is the maximum. In contrast for coupled consolidation, the excess pore water pressure increases to some peak value which is greater than the applied load and then dissipates gradually; this phenomenon is known as the Mandel- Cryer effect. This phenomenon was first studied by Mandel (1953) during the analysis of a saturated soil

cylinder under the axi-symmetric external load. Cryer 1963) also found a similar phenomenon in the consolidation of a soil ball with a uniform radial external load. Total stress variation during the consolidation is the cause of the Mandel- Cryer effect. The Mandel-Cryer effect does not appear in 1-D homogeneous soil consolidation where there is no lateral pore pressure dissipation and subsequent lateral deformation. Therefore, the variation of pore water pressure of coupled and uncoupled theory is equal to each other for saturated soil (Abid and Pyrah 1988). Huang and Griffiths (2010) compared the outcomes derived from Terzaghi's theory, Schiffman's 1970 uncoupled theory, and the coupled theory for one-dimensional saturated layered soil. The findings indicate that the results from Schiffman's (1970) uncoupled theory and the coupled theory were nearly identical, while Terzaghi's theory produced significantly different results.

The coupled consolidation theory was initially proposed for constant loading and later expanded to encompass various forms of time-dependent static loading (Schiffman, 1958). However, numerous natural phenomena (such as sea waves impacting waterfront structures, wind-induced oscillations on tall buildings and bridges, tidal variations, and storm waves) and human activities (including vehicular traffic on highways, airports, and railways, reciprocating machinery, filling and discharging of silos and water tanks, machinery vibrations, piling, movement of loads across factory floors or bridges and dynamic compaction) generate repeated or cyclic loading on the supporting soil. Highway engineers encounter numerous challenges stemming from cyclic loadings induced by vehicle traffic on roadways. Soil layers beneath these roads experience repeated load applications interspersed with periods of overburden pressure alone. While the duration of load application during traffic movement is typically brief, lasting only fractions of a second, intersections and parking areas may sustain loads for several minutes or even hours. Discrepancies between settlements predicted by theoretical models based on static loads

and those observed in field measurements underscore the necessity for investigating consolidation under cyclic loadings. The mechanisms of consolidation settlement under static and cyclic loading differ significantly, necessitating detailed and separate investigations. Wilson and Elgohary (1974) developed an analytical solution for consolidation under cyclic loading using the integral transformation technique. Baligh and Levadoux (1978) studied the consolidation of inelastic clay subjected to rapid cyclic loading through analytical and numerical methods. Favaretti and Mazzucato (1994) and Guan et al. (2003) provided analytical solutions for the consolidation of clays under triangular and trapezoidal loading, respectively. Conte and Troncone (2006, 2007) analyzed both linear and nonlinear consolidation processes for single and cyclic loads by selecting an appropriate period of the Fourier series. Toufigh and Ouria (2009) proposed a semi-analytical solution for rectangular cyclic loading on layered plastic clays, and Ouria et al. (2015) offered a simplified explanation based on the disturbed state concept (DSC) framework. Abbaspour (2014) provided numerical and experimental observations on the one-dimensional consolidation of clay under cyclic triangular loading, considering both linear and nonlinear theories. Consolidation settlement under haversine loading was further investigated using numerical techniques by Razouki and Schanz (2011) and analytical techniques by Razouki et al. (2016). More recently, Kim et al. (2020) obtained analytical solutions for consolidation in stratified soil considering trapezoidal, triangular, and rectangular loadings.

These studies typically simplified the drainage boundaries to either be fully drained (Dirichlet) type or fully undrained (Neumann) type. However, in reality, the drainage boundaries of consolidating layers are often partially drained, neither fully pervious nor completely impervious. This partial drainage occurs because the layers above and below the compressible zone possess certain thicknesses and permeability, affecting the drainage

surfaces. For example, in preloading projects on soft clay ground, if the drainage capability of the sand cushion at the clay boundary is inadequate (due to poor permeability), fine particles can clog the drainage path, hindering the discharge of air and water phases (Duncan 1993; Xie et al. 1999; Lei et al. 2016). This impeded drainage boundary influences the total settlement of the compressible layer, with the permeability of the impeded layer contributing to the overall settlement. To model partially permeable drainage boundaries, researchers have employed either a semipermeable boundary condition (where a non-dimensional parameter relates excess pore pressures and their spatial gradients) or an exponentially time-growing drainage boundary condition (where excess pore pressures decay exponentially over time through a parameter reflecting the dissipation rate at the boundary). Both approaches are generalized in nature. Impeded drainage boundaries have been considered in studies on saturated conditions (Gray 1945; Schiffman and Stein 1970; Mesri 1973; Xie et al. 1999; Liu and Lei 2013).

These investigations relied on the assumption of a linear correlation between fluid flow and hydraulic gradient, following Darcy's law. However, Darcy's law is inadequate for fine-grained, low-permeability soils, particularly when subjected to low hydraulic gradients, as explained in Chapter 4.

The present chapter deals with the combined effect of semipermeable drainage boundaries and non-Darcian fluid flow along with the time-dependent periodic loading on the 1-D consolidation saturated clayey soil. The semipermeable drainage boundary is modeled using a hypothetical impeded layer, while the influence of low hydraulic gradient is accurately represented by the four-parameter-dependent non-Darcian fluid flow law (Elnaggar et al. 1973). Numerical simulations utilize the Crank–Nicolson finite-difference implicit scheme. The combined impact of semipermeable drainage boundaries and non-Darcian flow is thoroughly investigated through isochrones and consolidating curves. The

presence of semipermeable drainage boundaries significantly affects the dissipation of pore water pressure during periodic loading.

5.2 PROBLEM STATEMENT

A fully saturated, homogeneous, and isotropic clay medium with infinite lateral extent (Fig. 5.1) is subjected to four different loadings: one constant loading and three periodic loadings, specifically trapezoidal (TL), triangular (TRL), and rectangular (RL) patterns, as depicted in Fig. 5.1. The soil layer is bounded by two semipermeable drainage boundaries. The hypothetical cushions impeding the drainage on the top and bottom surfaces have thicknesses h_T and h_B, respectively. The permeabilities are denoted as k_T and k_B, and the drainage of the clayey layer is directly proportional to the hydraulic conductivity of the impeded layer and inversely proportional to its thickness, as noted by Zhou et al. (2017). The derivations of the one-dimensional coupled theory equations, which govern the dissipation of pore water pressure (PWP) and deformation, are detailed in the Appendix C1. The analysis is performed with the aid of the Crank-Nicolson implicit method. This method provides a high order of accuracy and guarantees unconditional stability. The entire numerical simulations are performed by developing a code in *MATLAB* (Version 2018).

Governing differential equations:

$$\frac{\partial q}{\partial t}-\frac{\partial u}{\partial t}=\frac{k}{m_v\gamma_w}\left\{1-(1-a)\theta\left[\exp\left(\frac{-\theta}{i_1\gamma_w}\frac{\partial u}{\partial z}\right)\right]\right\}\frac{\partial^2 u}{\partial z^2} \tag{5.1a}$$

$$\frac{\partial q}{\partial t}-\frac{\partial u}{\partial t}=\frac{1}{m_v}\frac{\partial^2 s}{\partial z\partial t} \tag{5.1b}$$

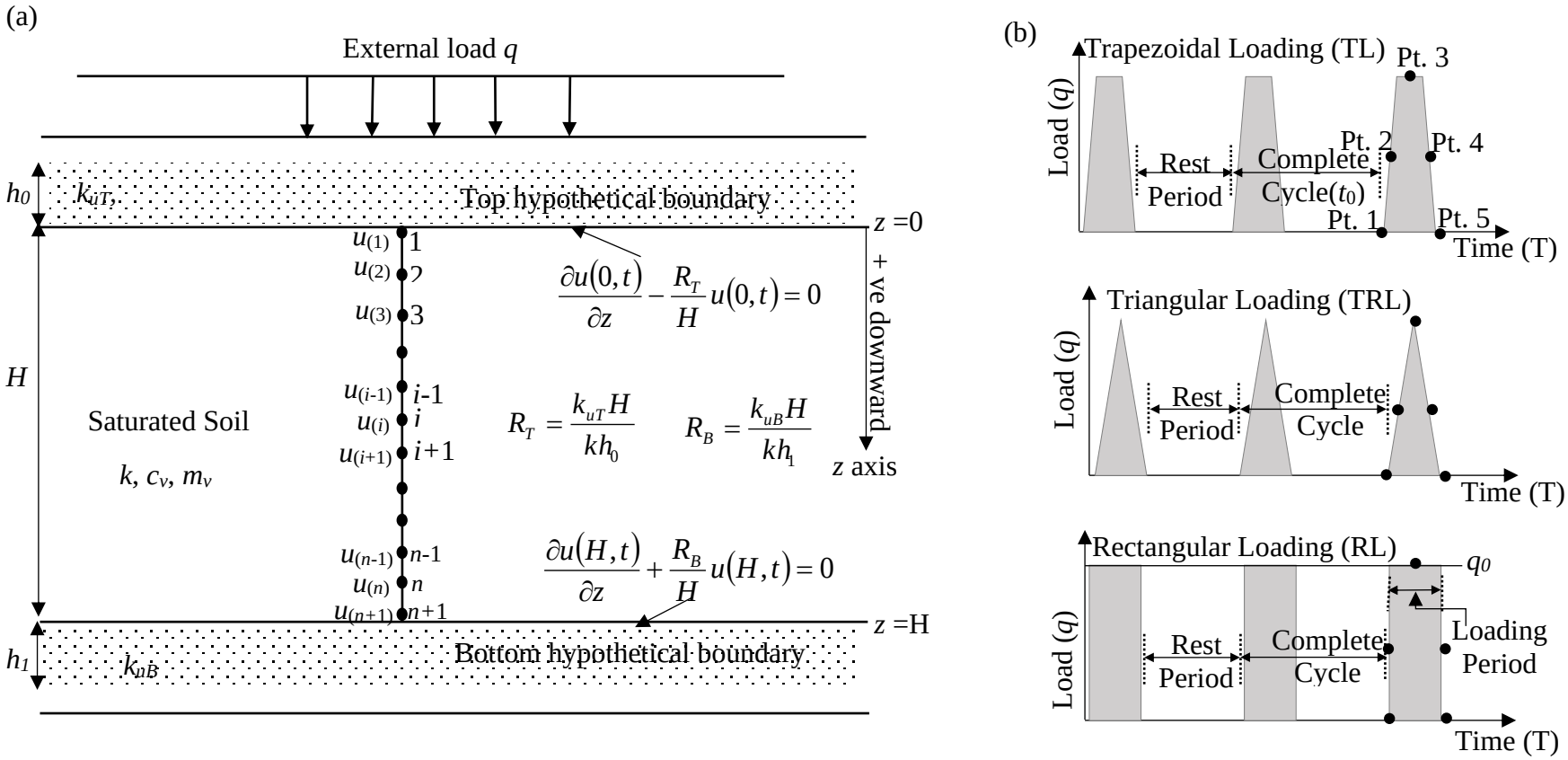

Fig 5.1 Schematic representation of the chosen (a) clay layer bounded by the semi-impermeable boundaries, and (b) applied periodic loading

Subjected to

Initial condition : u (z,0)=q, and $\frac{\partial s}{\partial z}=0$ where s is settlement of soil (5.2)

boundary conditions

Top boundary $\frac{\partial u(0,t)}{\partial z}-\frac{R_T}{H}u(0,t)=0$ where $R_T=\frac{k_T H}{k h_T}$ (5.3)

Bottom boundary $\frac{\partial u(0,t)}{\partial z}+\frac{R_B}{H}u(0,t)=0$ and s=0 where $R_B=\frac{k_B H}{k h_B}$ (5.4)

R_T and R_B are the drainage parameters on the top boundary and bottom boundary, respectively. These two parameters combindely referred to as the *R*-value. A fully pervious boundary condition is achieved when the corresponding semipermeable parameter approaches infinity. Conversely, a drainage boundary becomes completely impervious when the corresponding *R*-value is set to zero. Therefore, the impeded boundary condition is considered a generalized form of the boundary condition; Dirichlet (pore pressures = 0) and Neumann (pore pressure gradients = 0) boundary conditions can be obtained by adjusting the drainage parameters. The current study aims to investigate the impact of non-Darcian flow on the consolidation behaviour of a clayey stratum bounded by semipermeable layers under cyclic loading. The previous literature indicates that for homogenous soil, regardless of the load-type, flow type, and other influences, the coupled and uncoupled theory provide the same pore pressure profiles as long as the dissipation and deformation is one-dimensional. It is noteworthy that due to the one-dimensional nature of the problem Biot's coupled equations will be degenerated to a single diffusion equation, as demonstrated earlier by Abid and Pyrah (1988) and Huang and Griffith (2010). Hence, in true sense of term, Eqs. 5.1a and 5.1b cannot be treated as a coupled form. Eq. 5.1a provides $u(z,t)$ which further helps in evaluating the settlement s(z,t) profiles from Eq. 5.1b. The major benefit of solving the second equation along with the dissipation equation (Eq. 5.1a) is to directly predict the local deformation and global settlement without relying on the

conventional degree of consolidation curve which are associated with the pore pressure values.

5.3 NUMERICAL ANALYSIS

The consolidating layer is divided into (n + 1) equally spaced grid points, as shown in Fig. 5.1. To determine the spatial and temporal variations of u, Eqs. (5.1a) and (5.1b) must be solved simultaneously at each grid point.

$$\left(\frac{\partial q}{\partial t}-\frac{\partial u}{\partial t}\right)\Bigg|_i = \frac{k}{m_v\gamma_w}\underbrace{\left\{1-(1-a)\theta\left[\exp\left(\frac{-\theta}{i_1\gamma_w}\frac{\partial u}{\partial z}\right)\right]\right\}}_{E_i^t}\frac{\partial^2 u}{\partial z^2} \tag{5.5}$$

According to the CN scheme, the PDEs at any arbitrary grid point

$$\left(\frac{\partial q}{\partial t}-\frac{\partial u}{\partial t}\right)\Bigg|_i = \frac{0.5k}{m_v\gamma_w}E_i^t\left(\frac{\partial^2 u}{\partial z^2}\Bigg|_i^{t+\Delta t}+\frac{\partial^2 u}{\partial z^2}\Bigg|_i^{t}\right) \tag{5.6a}$$

$$\left(\frac{\partial q}{\partial t}-\frac{\partial u}{\partial t}\right)\Bigg|_i = \frac{0.5}{m_v}\left(\frac{\partial^2 s}{\partial z\partial t}\Bigg|_i^{t+\Delta t}+\frac{\partial^2 s}{\partial z\partial t}\Bigg|_i^{t}\right) \tag{5.6b}$$

To eliminate the nonlinearity in Eq. (5.6a), the spatial gradient of u in the exponent term is evaluated at the previous (known) time step. Each internal grid point must comply with the governing differential equations, while the boundary grid points must satisfy the following constraints:

Top boundary	Bottom boundary
$\left.\frac{\partial u}{\partial z}\right\|_{z=0}-\frac{R_T}{H}u\big\|_{z=0}=0$	$\left.\frac{\partial u}{\partial z}\right\|_{z=H}+\frac{R_B}{H}u\big\|_{z=H}=0$
$\frac{u_2^{t+\Delta t}-u_0^{t+\Delta t}}{2\Delta z}-\frac{R_T}{H}u_1^{t+\Delta t}=0$	$\frac{u_{n+2}^{t+\Delta t}-u_n^{t+\Delta t}}{2\Delta z}+\frac{R_B}{H}u_{n+1}^{t+\Delta t}=0$
$u_2^{t+\Delta t}=u_0^{t+\Delta t}+2\Delta z\frac{R_T}{H}u_1^{t+\Delta t}$	$u_{n+2}^{t+\Delta t}=u_{n+1}^{t+\Delta t}-2\Delta z\frac{R_B}{H}u_n^{t+\Delta t}$

The Crank–Nicolson (CN) scheme transforms the partial differential equations (PDEs) into simultaneous sets of linear algebraic equations. The forward and central difference techniques are employed to discretize the differential terms associated with time (first-order) and space (second-order), respectively. The formation of these algebraic equations for each node, along with the resulting coefficient matrix, is detailed in Appendix C2. In this analysis, Δz and Δt represent the user-defined depth and time increments, respectively. For the current study, 100 segments (n) are chosen, making Δz equal to 0.1 m. Additionally, Δt is set to 100 seconds. These increments are selected based on the criterion that further refinement does not significantly impact the computed solutions.

5.4 RESULTS AND DISCUSSIONS

The analysis presents the variation of computed field variables PWP (u) during the consolidation process, providing both local and global information in three distinct forms: normalized isochrones, the average degree of consolidation (also known as representative settlement curves), and the degree of consolidation at various specific points. Coupled consolidation analysis also provide the facility to calculation of deformation progress throughout the entire layer over time.

5.4.1 Constant loading

Figs. 5.2, 5.3, and 5.4 demonstrate the impact of non-Darcian flow model parameters on the dissipation of PWP and settlement of soil for constant loading. Different combinations of model parameters a (= 0.1, 0.5, and 0.9), θ (= 0.1, 0.5, and 1), and i_1 parameters (= 5 and 45) are selected for the analysis. The dashed line of the figures shows the Darcian flow (DF), while the dotted line represents the non-Darican flow (NDF).

Fig. 5.2 depicts the normalized isochrones (normalized with respect to load) plotted at three different time intervals (namely, 1.3×10^6 sec., 2.6×10^6 sec. and 7.8×10^6 sec.) corresponding to $R_T = \infty$ and $R_B = 10$. At the top of the clay layer, the R_T is infinite, indicating

a fully permeable boundary, which results in the pore water pressure (PWP) being zero at the top surface. Conversely, at the bottom of the clay layer, the R_B is 10. This means the bottom boundary is neither fully permeable (where the isochrones would be zero) nor completely impermeable (where the isochrones would be perpendicular to the surface). Instead, the isochrones at the bottom boundary have a value greater than zero. Another observation that can be made from Fig 5.2 is that the impact of model parameters is the same as the conventional boundary condition (Chapter 4). Higher flow nonlinearity (i.e., lower a and/or higher θ) results in a slower consolidation process, with θ having a more significant impact than a. The variation in i_1 shows negligible visual impact on the plotted isochrones. As time increases, the difference between DF and NDF increases, and the maximum difference is found in the middle portion of the consolidating layer.

Fig 5.3 shows the U_{avg} with respect to the consolidation time graph for constant loading. The graphs are plotted for three different sets of symmetric R-values (R_T= R_B). They are: R=∞, R=1, and R=5. It is to be noted represent PTPB condition. The impact of non-Darcian flow are also shown in this figure; the model parameters are the same as the previous figure i.e. a (= 0.1, 0.5, and 0.9), θ (= 0.1, 0.5, and 1), and i_1 parameters (= 5 and 45). The effect of model parameters are same on the U_{avg} vs t graph as isochrone. Fig 5.3 reveals that as the R-value decreases, the rate of consolidation decreases, and the curve shifts towards the right side. Another observation also can be made that as the R-value decreases, the time difference between DF and NDF for a certain amount of consolidation increases.

Fig. 5.4 illustrates the settlement (s) at the top of the soil layer normalised with respect to s^* ($s^* = m_v.q_0.H$) throughout the consolidation. The settlement of the clay layer is maximum at the top (z=0) and zero at the bottom (z=H). The graphs depict three different sets of symmetric R values: the first under PTPB conditions (R = ∞), and the other two with

R values of 1 and 5. The impact of non-Darcian parameters are also shown. The model parameters are the same as those in the previous U_{avg} vs *t* curve. The figure reveals that the shape of the settlement curve for the constant loading is the same as the degree of the consolidation curve.

5.4.2 Cyclic loading

Figs 5.5-5.13 illustrate the impact of cyclic loading on soil consolidation. It comprehensively discusses the effects of symmetric and asymmetric *R*-values on different cyclic loading, the ratio of loading time to rest period (η), and the cycle time (t_0) on soil consolidation and settlement. The black solid line represents consolidation assuming Darcian flow (DF), whereas the green dashed line represents consolidation due to non-Darcian flow (NDF). Figs. 5.5, 5.8, and 5.10 represent the variations of U_{avg} with the time, different loadings, and drainage conditions. The graphs reveal that, unlike constant loading, the magnitude of U_{avg} oscillates with time under periodic loading. It can be interpreted practically as the occurrence of both compression and swelling within the entire consolidating layer. In the initial stage of consolidation, compression of the layer is more pronounced, but as the loading and unloading cycles continue, the soil reaches a state where it begins to rebound completely. It can be attributed to the elastic state, also known as the steady-state condition under cyclic loading. Once this steady state is achieved, the soil mass can no longer undergo further consolidation, and the magnitudes of compression and swelling remain consistent with each loading cycle. This phenomenon can be explained by the generation and dissipation of positive excess pore water pressure (PWP) due to the expulsion of pore water when the load is applied. Conversely, the removal of the additional applied pressure creates negative excess PWP, which causes the water to flow back into the consolidating layer. Initially, positive excess PWP predominates, leading to more water expelled from the stratum.

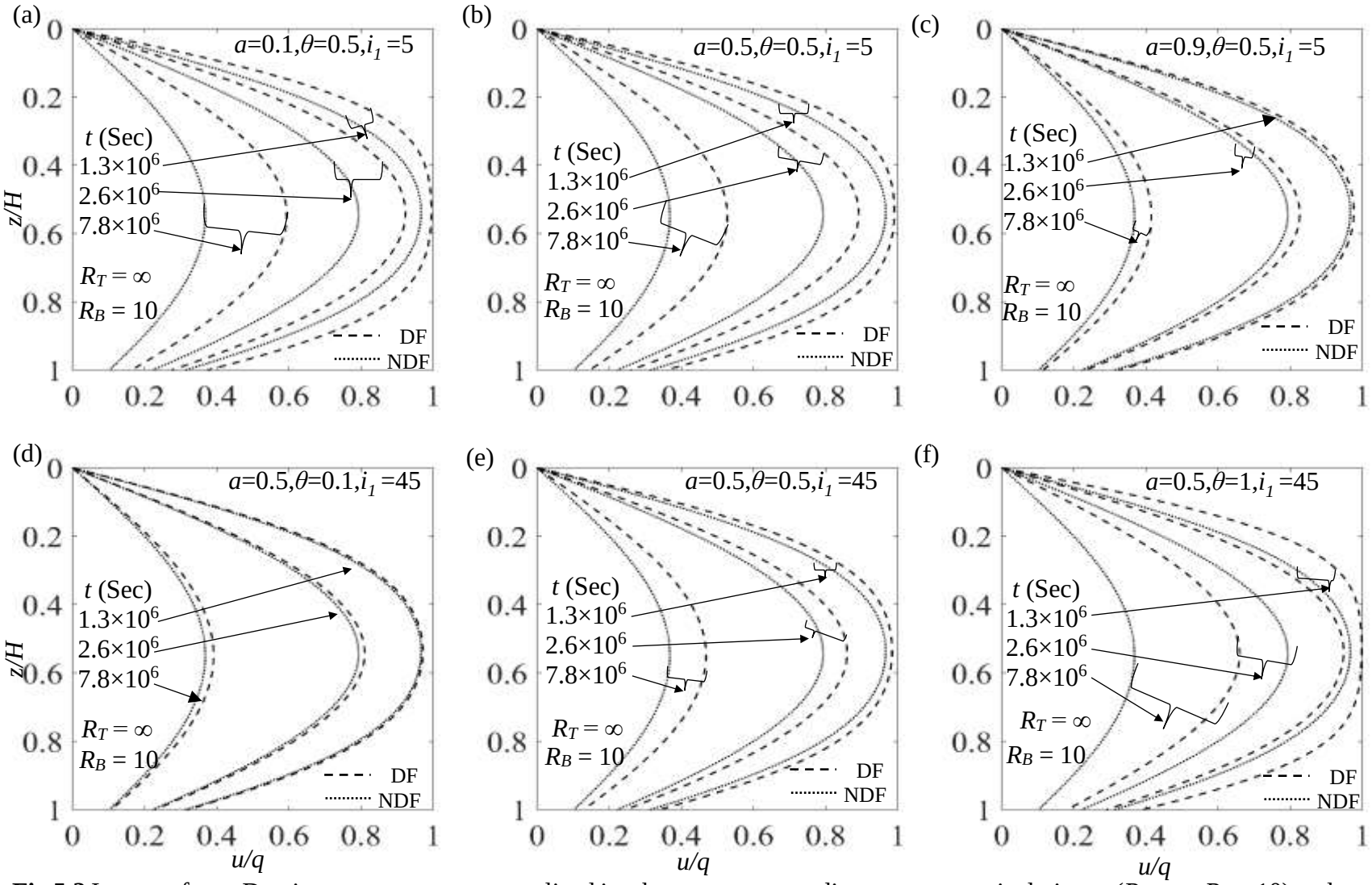

Fig 5.2 Impact of non-Darcian parameters on normalized isochrones corresponding to asymmetric drainage ($R_T = \infty$, $R_B = 10$) and constant loading.

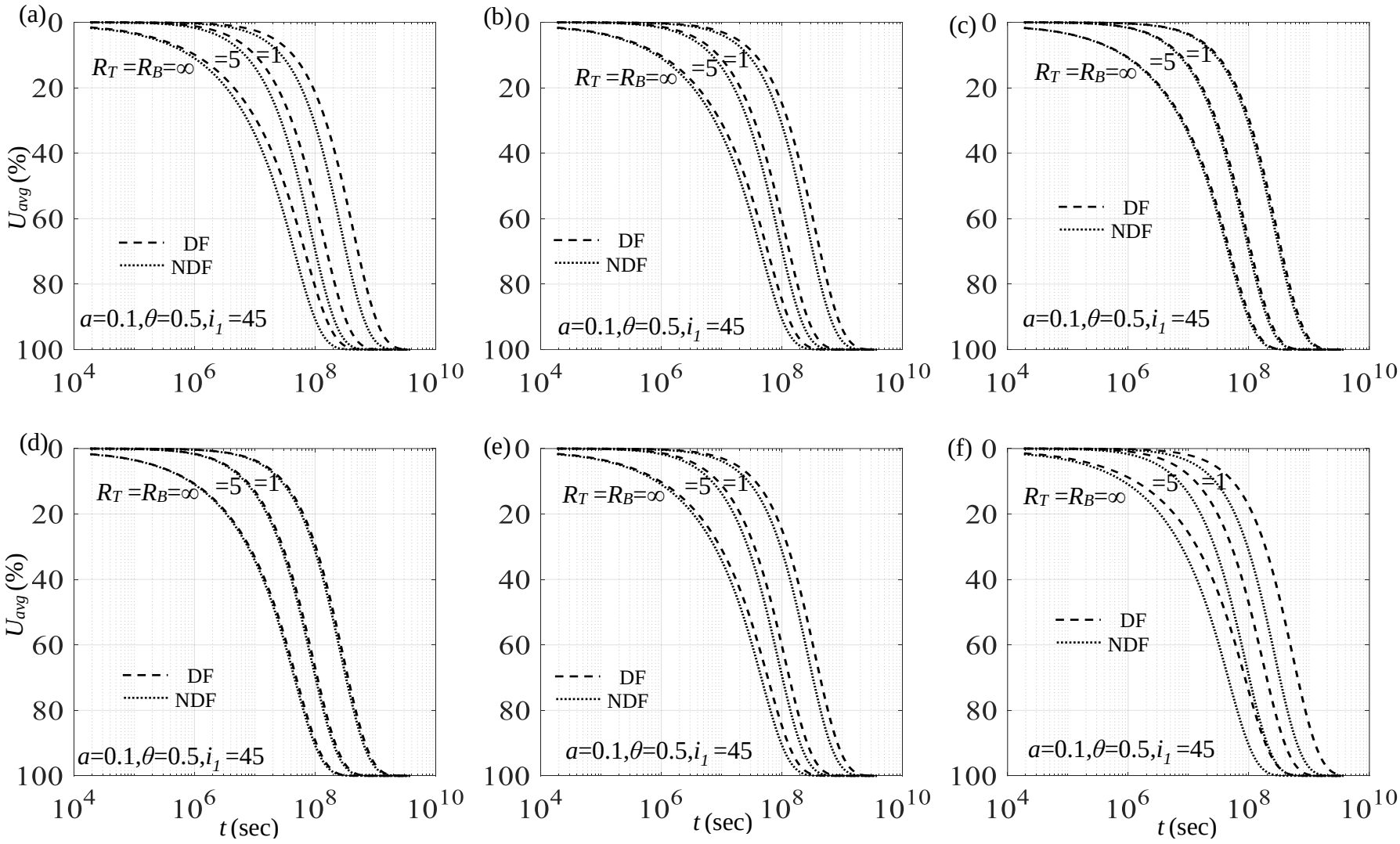

Fig 5.3 Impact of non-Darcian parameters on consolidation curves corresponding to symmetric drainage ($R_T = R_B = \infty$) and constant loading.

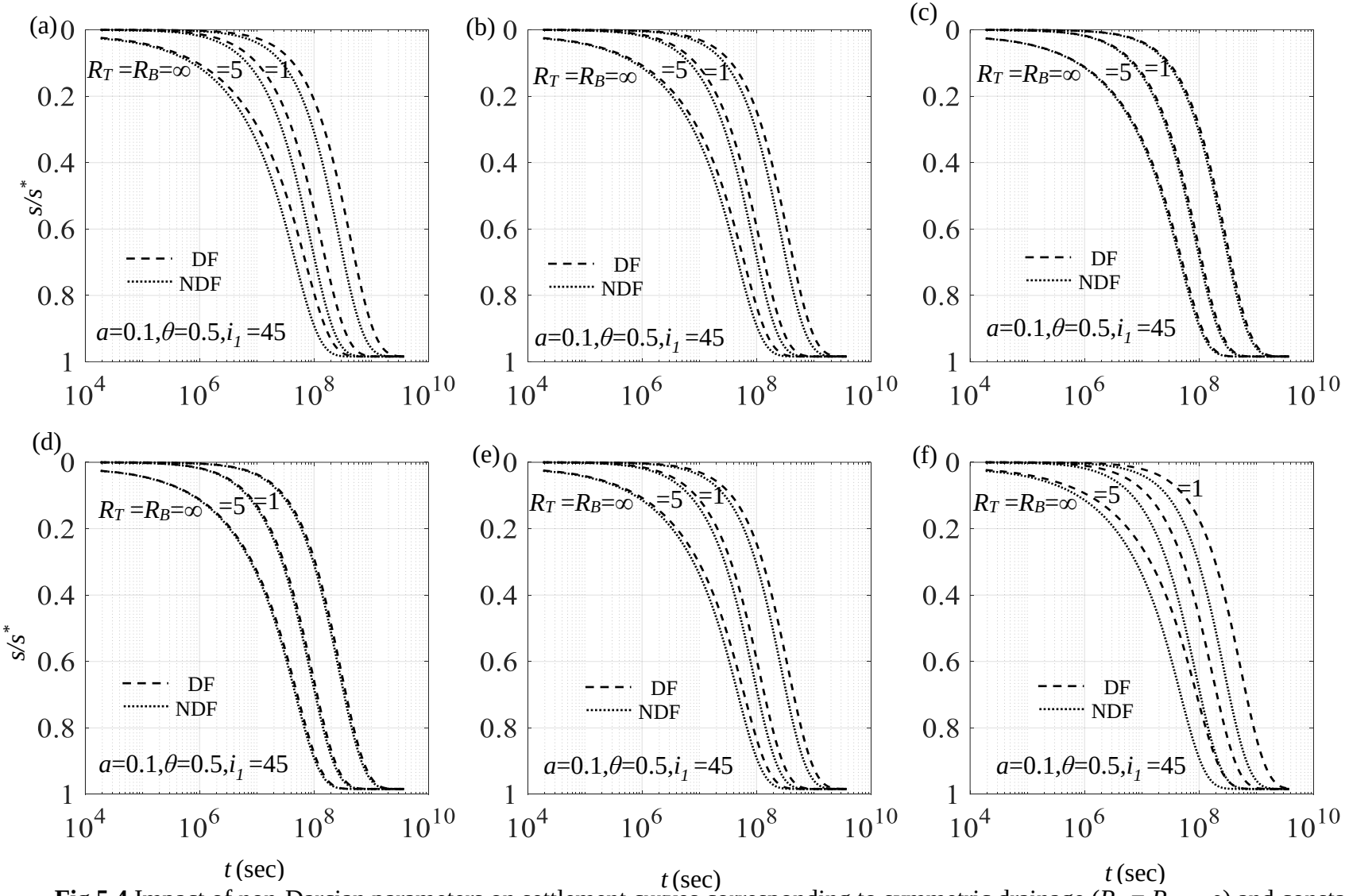

Fig 5.4 Impact of non-Darcian parameters on settlement curves corresponding to symmetric drainage ($R_T = R_B = \infty$) and constant loading.

As the loading and unloading cycles continue, the system reaches a state where the excess PWP and effective pressure reach final equilibrium values. In this equilibrium state, the amount of water flowing out due to the positive excess PWP becomes equal to the amount of water flowing within the soil due to the negative excess PWP.

The width of the elastic state after reaching equilibrium in the U_{avg} vs. t graph can be represented by $D_{u,}$ while the time required to reach equilibrium is denoted by t_e. Another observation from the figures is that the peak of the consolidation curve and the peak of the loading curve do not necessarily occur simultaneously.

Fig. 5.5 shows the impact of boundary parameters R_T and R_B for different types of loading (TL, TRL, and RL) along with non-Darcian flow. It is assumed that the ratio (η) of loading and rest period is 2, and time for the complete cycle (t_0) is 5×10^5 sec, and the value of model parameters a=0.1, θ=1, and i_1 are 45. The top boundary is chosen to be the previous (R_T=∞), while three different R_B (∞, 5 and 0) are taken for the analysis. Fig 5.5 shows that regardless of the flow law, as the boundary condition shifts from impervious to previous D_u decreases for TL and RL, but increases for TRL. Further, the rate of decrease of D_u is significantly higher in RL compared to TL. Another observation from the figure is that for TL and RL, D_u is greater for Darcian flow compared to non-Darcian flow, whereas for TRL, the opposite characteristic is manifested. Fig 5.5 also shows that t_e for NDF is always greater than its Darcian counterpart. The R-value of the boundary also affects the magnitude of t_e. Whatever the applied loading and flow types, t_e increases with decreasing R. For PTIB, the consolidation curve resembles the loading pattern, particularly evident during the first cycle for NDF.

Fig 5.6 shows the normalized settlement curve drawn for both Darcian and non-Darcian flow for various cyclic loading. The upward direction of deformation shows the swelling of the soil, which occurs during the unloading because of the generation of pore

water pressure, and a downward direction of deformation shows the settlement of the soil, which is caused by the dissipation of PWP. Like the consolidation curve, the deformation curve for periodic loading also oscillates and attains the equilibrium state during consolidation. The extent of the elastic deformation (in the normalized deformation vs t graph), at the equilibrium state, can be represented by D_s. The graphs are drawn for η=2, t_0=5×10^5 sec, a=0.1, θ=1, and i_1 = 45. Fig. 5.6 demonstrates that in the deformation curves for TL and RL, the D_s value for Darcian flow is higher than that for non-Darcian flow. However, under triangular loading, the D_s value for non-Darcian flow exceeds that for Darcian flow. The difference in the width of the elastic state for the deformation curve between DF and NDF is greater than the difference in the width of the elastic state at equilibrium for the consolidation curve between DF and NDF. Fig. 5.6 also shows that the value of D_s is largest for the rectangular loading. Nevertheless, for the PTIB condition, D_s decreases for all the periodic loadings. The deformation curve also resembles the loading pattern, especially observed in the first cycle.

Fig 5.7 illustrates the impact of boundary conditions on the normalised pore water pressure profiles drawn at different positions of the soil layer (h/H=0.2, 0.5, and 0.8) subjected to trapezoidal loading. Fig 5.7 is drawn for three different R_B values (∞, 5 and 0) while R_T is taken to infinite. It can be observed that the difference in width of static equilibrium between DF and NDF is maximum at the center of the clay layer for all the boundary conditions. As R_B decreases (indicating the boundary moving towards imperviousness), the width of the elastic state at equilibrium for the pore water pressure curve diminishes yet the time needed to reach the equilibrium condition increases as R_B decreases. Another notable observation is that when the bottom boundary is impervious (R_B=0), the pore pressure curve near the bottom (h/H=0.8) closely mirrors the loading pattern not only for the first cycle but for multiple cycles.

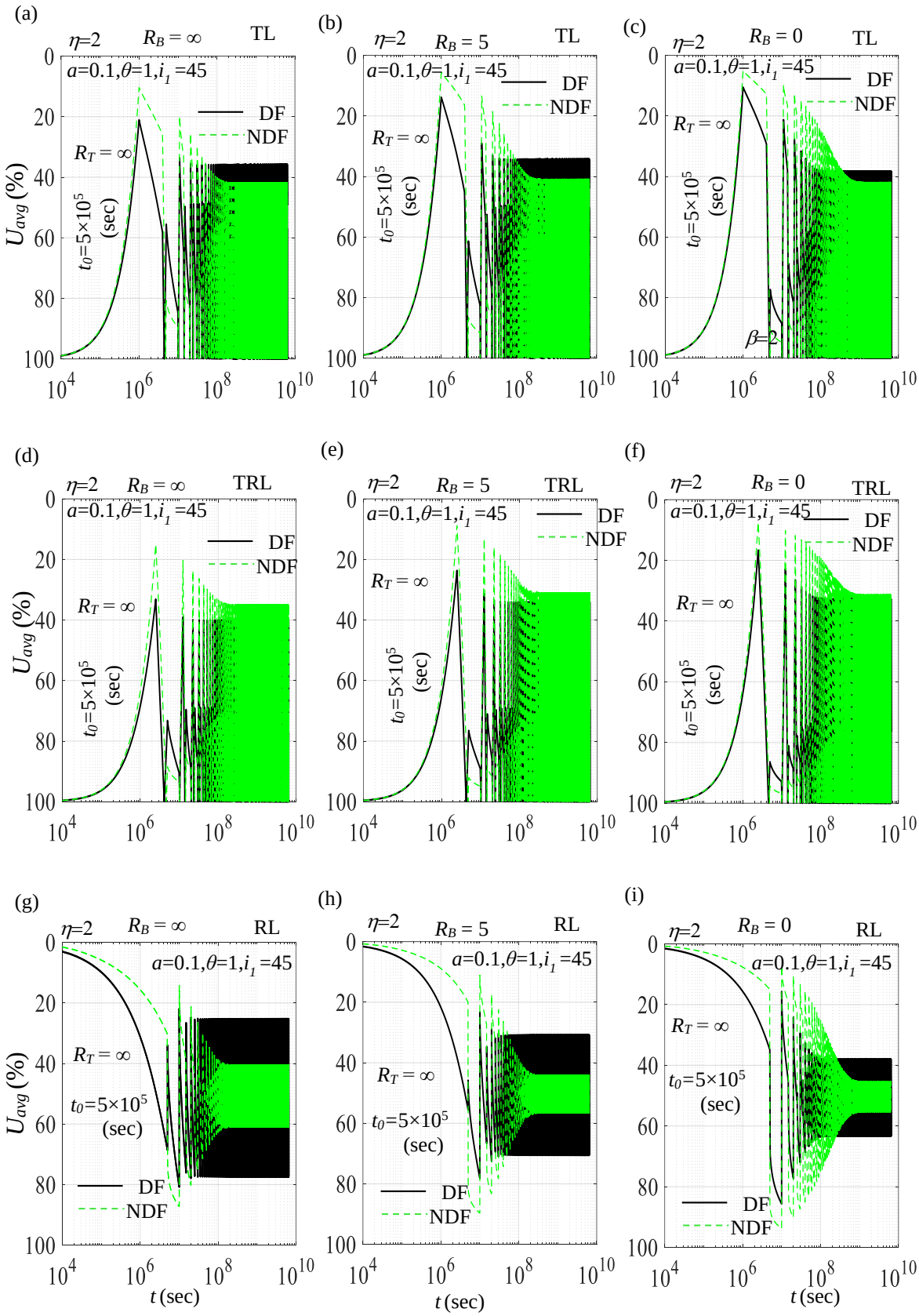

Fig 5.5 Impact of non-Darcian and asymmetric boundary conditions on the consolidation curves for the chosen periodic loadings: (a-c) TL, (d-f) TRL, and (g-i) RL.

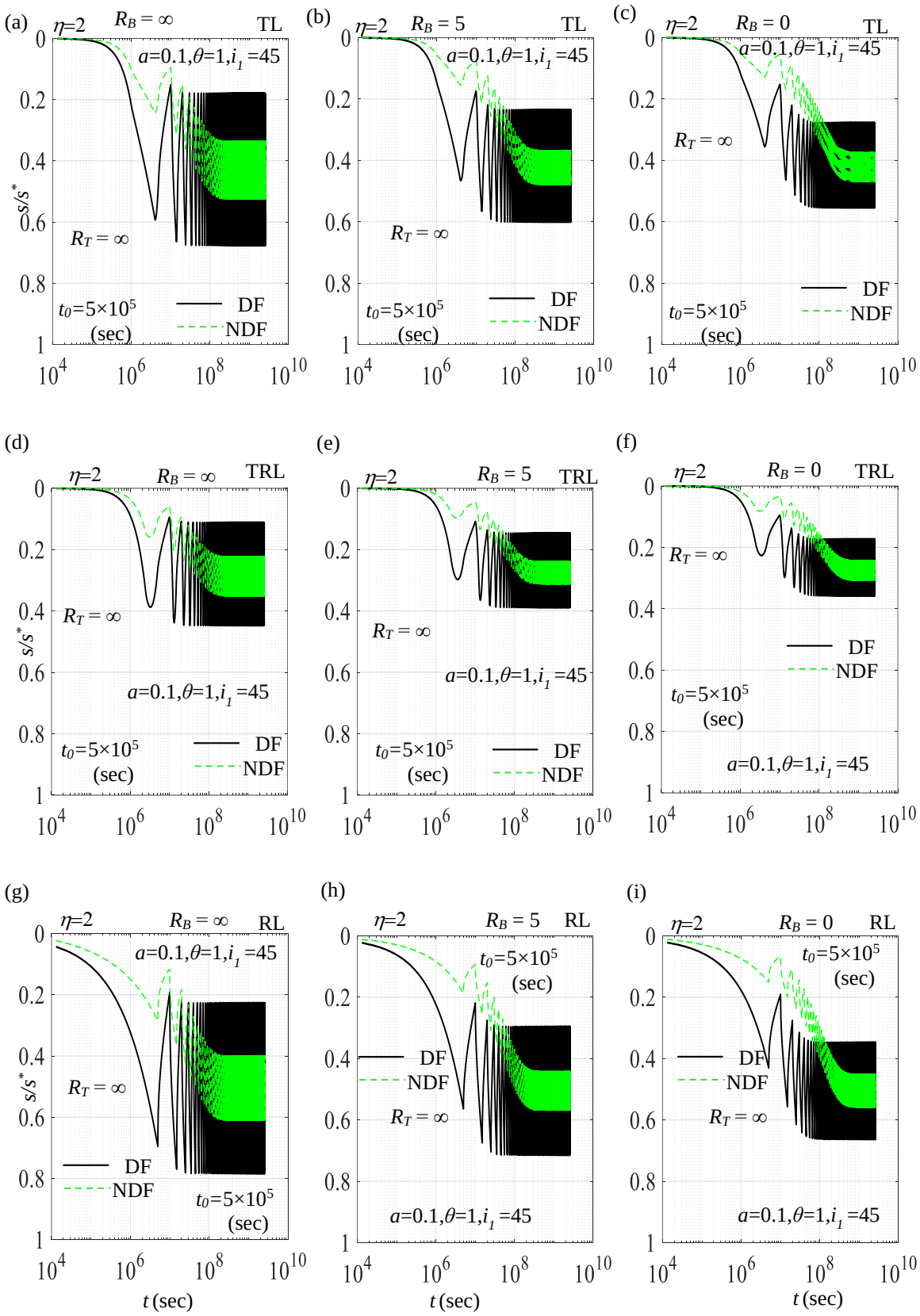

Fig 5.6 Impact of non-Darcian and asymmetric boundary conditions on the settlement curves for the chosen periodic loadings: (a-c) TL, (d-f) TRL, and (g-i) RL

Fig 5.8 shows the impact of symmetric boundary conditions (R_T=R_B) on the U_{avg} vs t curve. Three different symmetric R-values (10, 5, and 1) and t_0= 5×10^5 sec and η=2 are chosen for the analysis. From Fig 5.8, it can be observed that similar to the asymmetric case, the D_u for TL and RL is greater for Darcian flow than for non-Darcian flow while the opposite behaviour is observed for TRL. Another observation can be made that the rate of decrease in D_u with the decrease in R-value is much higher for RL compared to TL and TRL. However, for all the periodic loading, the difference in D_u between the Darcian and non-Darcian flow shrinks continuously with the decrease in R.

Fig. 5.9 shows the settlement curve for three symmetrical R-values (10, 5, and 1) pertaining to η=2, and t_0= 5×10^5 sec. Fig 5.9 demonstrates that D_s decreases with a decrease in R-value for both Darcian and non-Darcian flow. The difference in D_s between Darcian and non-Darcian flow increases for TL as the boundaries become undrained (low R-value). Fig. 5.10 reveals the combined impact of loading pattern and cycle time (t_0) on the consolidation rate for both Darcian and non-Darcian flow. Three values of t_0 (10^7, 5×10^7, and 10^8 seconds) are chosen for the analysis. The parameters η = 2, a = 0.1, θ = 1, and i_1 = 45 are used in the current analysis. Fig. 5.10 shows that for both TL and TRL, as t_0 increases, the value of D_u decreases for both Darcian and non-Darcian flow. The rate of decrease in D_u is much less in non-Darcian flow compared to Darcian flow. One interesting observation regarding the combined effect of loading type and t_0 can be made from Fig. 5.10. For TL, the value of D_u for non-Darcian flow is less than that for Darcian flow at t_0 = 10^7 seconds, but on further increment of t_0, D_u for non-Darcian flow surpasses the Darcian flow, indicating that t_0 significantly affects the type of flow for TL. The figure also illustrates that for TRL loading, the D_u of Darcian flow is consistently less than that of non-Darcian flow. However, RL exhibits a completely different behavior from TL and TRL.

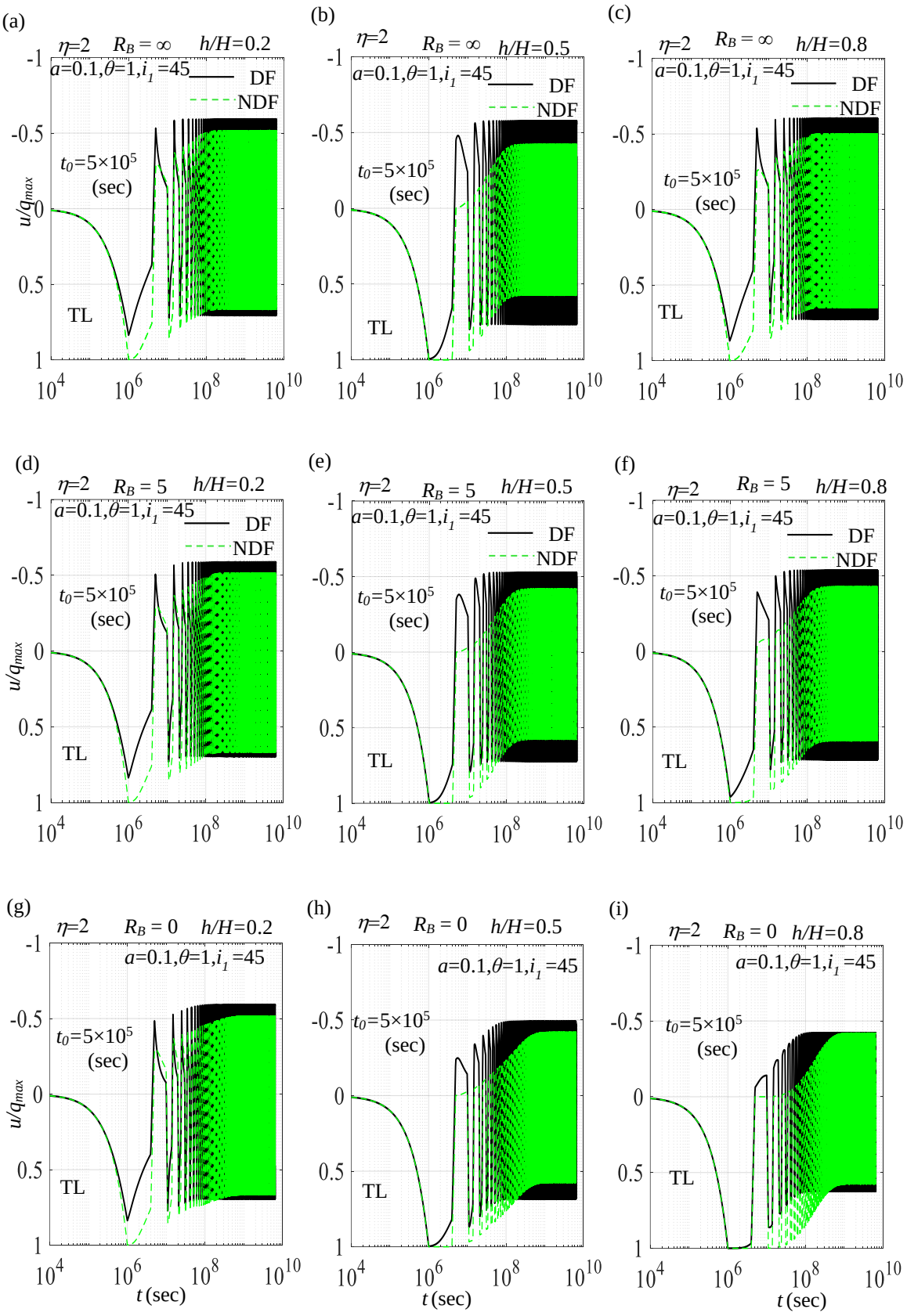

Fig 5.7 Impact of non-Darcian parameters on the PWP profiles at three different locations (h/H = 0.2,0.5 and 0.8) subjected to TL, $R_T = \infty$, and R_B equals to (a-c) ∞, (d-f) 5, (g-i) 0.

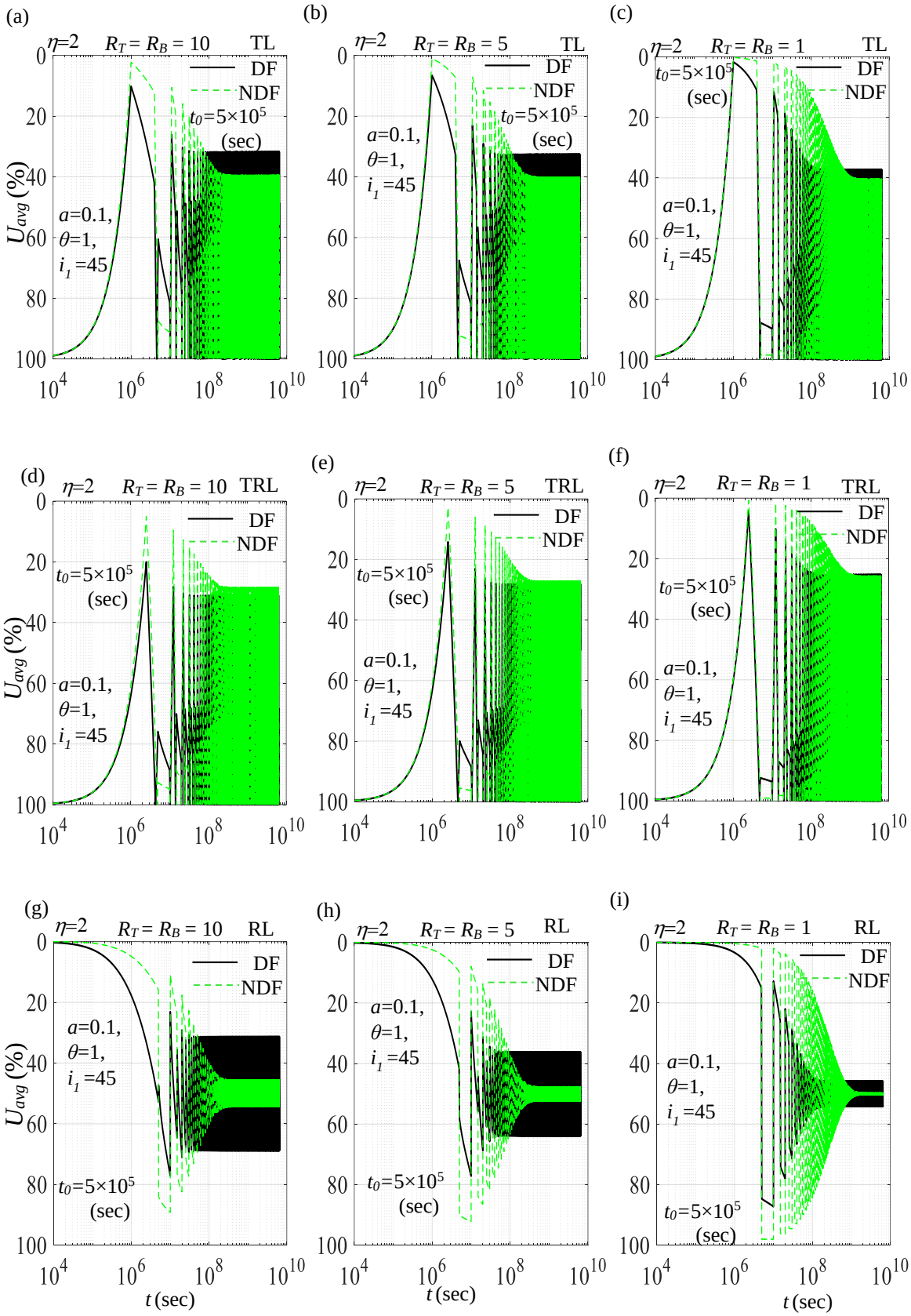

Fig 5.8 The consolidation curves subjected to nonlinear flow, different symmetric boundaries (R=10, 5, and 1), and periodic loadings: (a-c) TL, (d-f) TRL, and (g-i) RL.

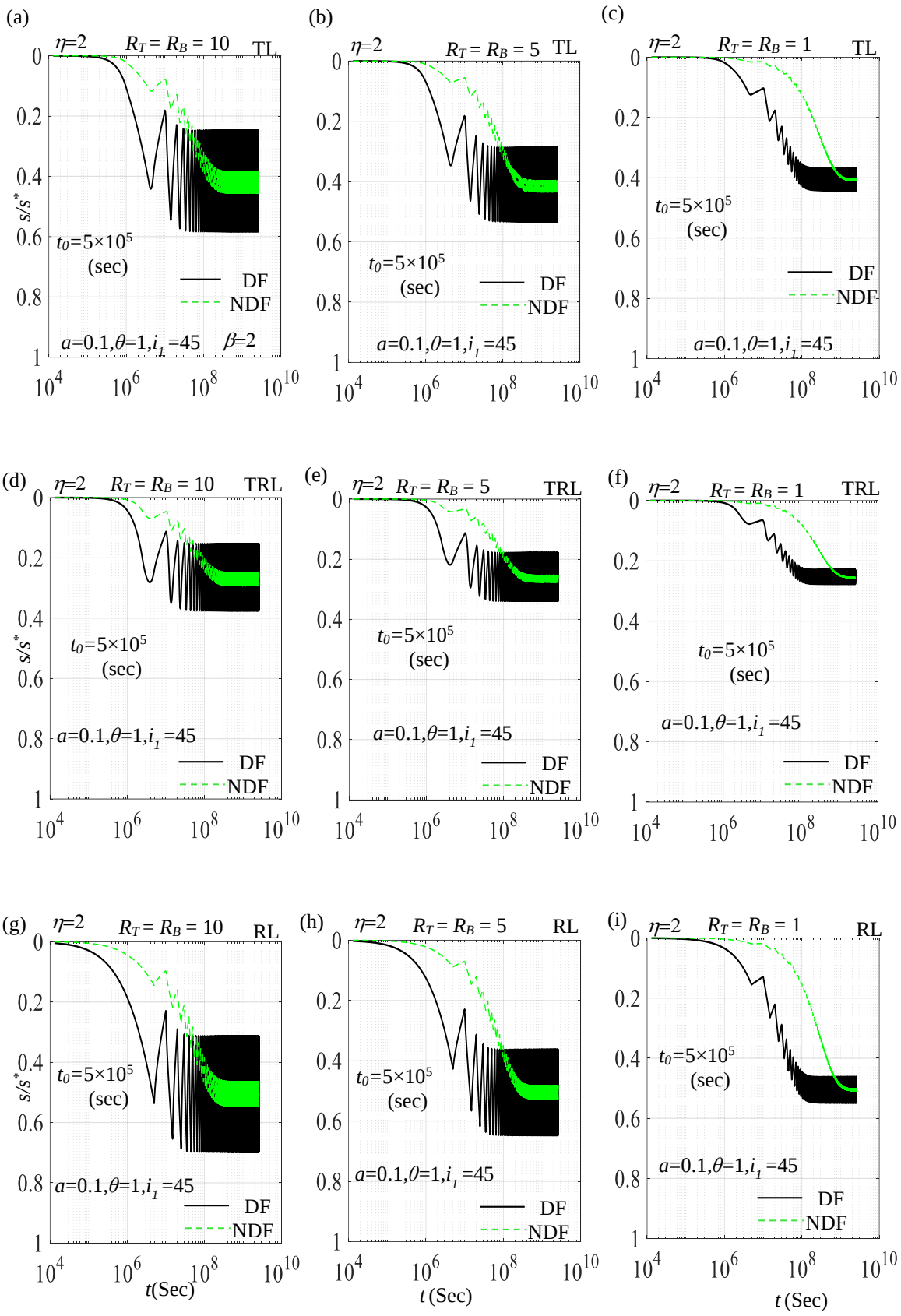

Fig 5.9 The normalized settlement curves subjected to nonlinear flow, different symmetric boundaries (R=10, 5, and 1), and periodic loadings: (a-c) TL, (d-f) TRL, and (g-i) RL.

In RL, as the value of t_0 increases, the D_u for both DL and NDL increases. Additionally, for RL loading, the D_u of DF is always greater than that of NDF.

Fig. 5.11 illustrates the impact of t_0 on the settlement curve for different loading conditions in both Darcian and non-Darcian flow. Three sets of t_0 values (10^7, 5×10^7, and 10^8 sec) along with three different symmetric R-values 10 are selected for the analysis. The other model parameters are: a=0.1, θ=1, i_1=45, and η=2. Fig. 5.11 shows that for all the periodic loading, D_S increases over time. However, the rate of decrease in D_S is significantly higher for Darcian flow compared to non-Darcian flow.

Fig 5.12 illustrates the combined effect of η and R_B on D_u under different periodic loading for both DF and NDF. The analysis utilizes the model parameters a=0.1, θ=1, and i_1=45, with t_0 set to 5×10^5 sec and R_T equals infinity. A common trend observed across all types of loading is that as the value of η increases, D_u initially decreases to a certain point, then starts to increase and eventually becomes constant. Additionally, as the value of R_B increases, D_u increases up to a certain point and then remains constant for both TL and RL. TRL exhibits the opposite behaviour: D_u of TRL decreases with an increase in R_B up to a certain point, after which it remains constant. The figure reveals that D_u for NDF is consistently smaller than for DF under TL and RL for the given T_0. However, for TRL, D_u of NDF is greater than DF across all values of R_B. Fig. 5.13 illustrates the combined impact of T_0 and symmetric boundary conditions on D_u for trapezoidal loading. The analysis uses the model parameters a=0.1, θ=1, and i_1=45, with t_0 set to 5×10^5 sec. The figure reveals that as the R-value increases, D_u decreases to a certain point and then remains constant. Additionally, it can be observed that as the value of t_0 increases, D_u initially increases up to a certain limit, but beyond that, further increases in t_0 result in a decrease in D_u. Another observation from Fig. 5.13 is that with increasing t_0, D_u for Darcian flow is initially greater

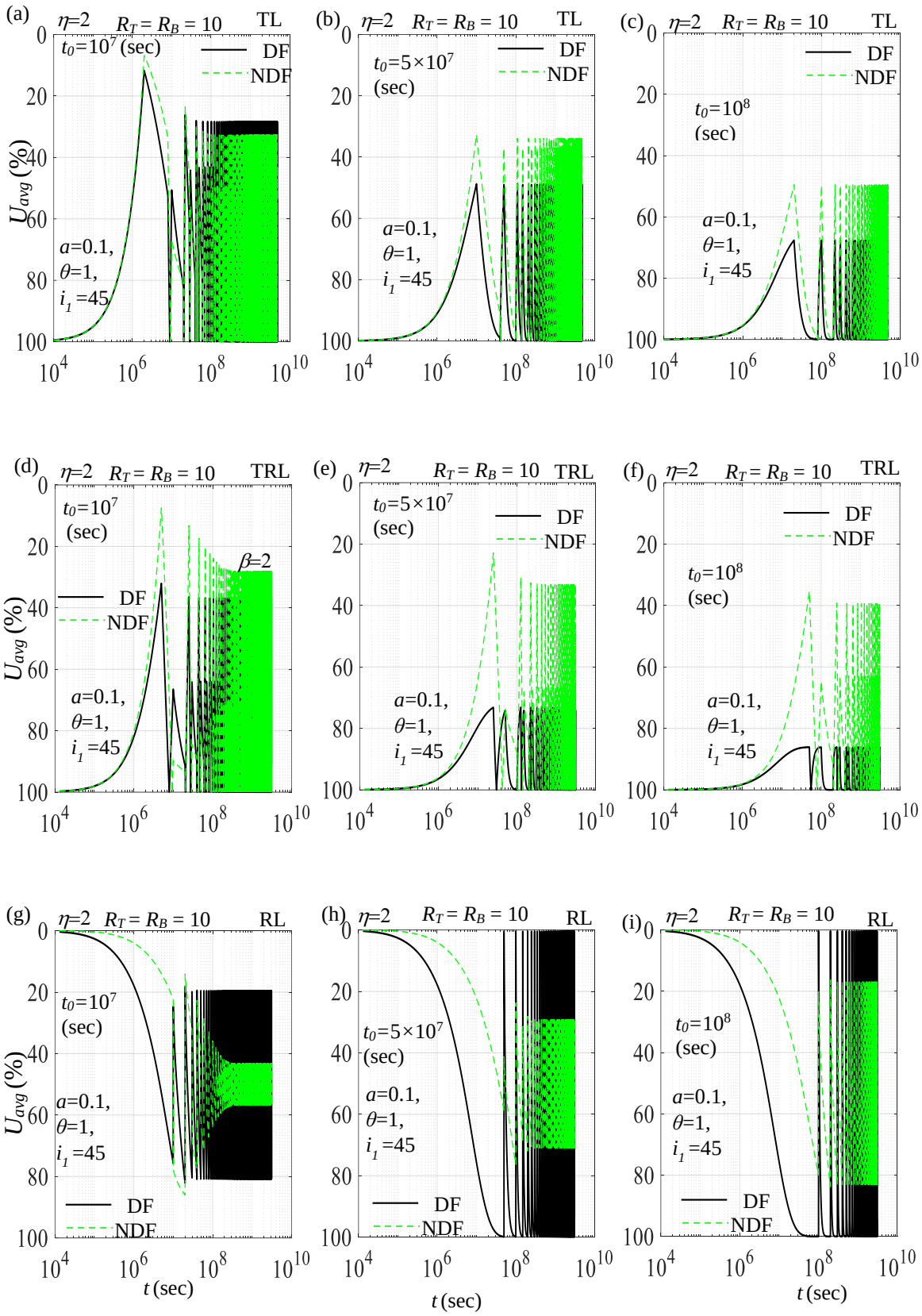

Fig 5.10 The consolidation curves subjected to different loadings (a-c) TL, (d-f) TRL, and (g-i) RL with different cycle times (T_0): (a,d,g) 10^7 *s*, (b,e,h) 5x10^7 *s*, and (c,f,i) 10^8 *s*.

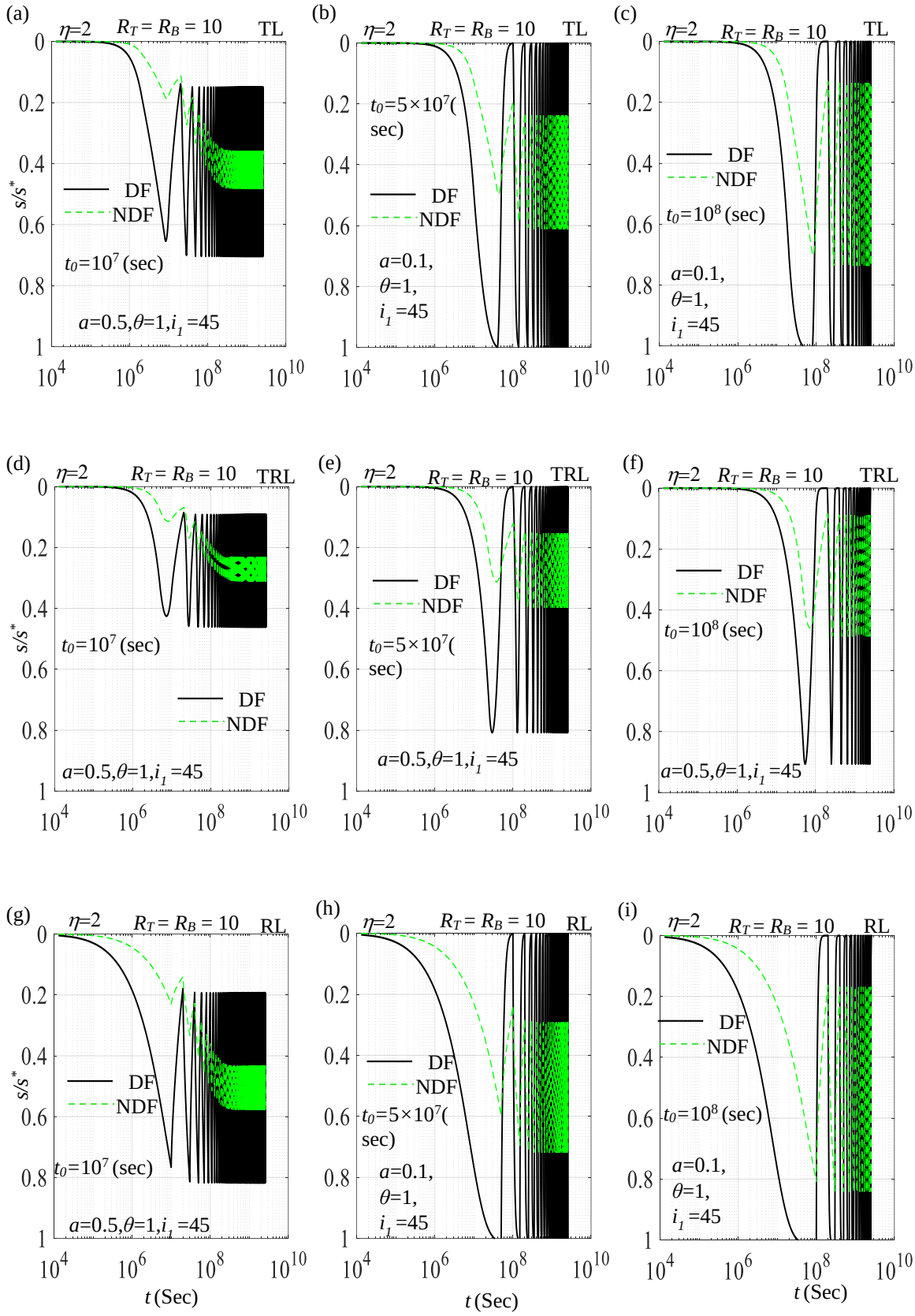

Fig 5.11 The settlement curves subjected to different loadings (a-c) TL, (d-f) TRL, and (g-i) RL with different cycle times (T_0): (a,d,g) 10^7 s, (b,e,h) 5x10^7 s, and (c,f,i) 10^8 s.

than for non-Darcian flow. However, after a certain t_0 value, D_u for non-Darcian flow surpasses that of Darcian flow and remains higher.

Fig. 5.14 displays isochrones at five different time points, as illustrated in Fig. 5.1b. Point 1 represents the end of the rest period and the beginning of the loading period, with q being zero at that point. Point 2 signifies the loading period where q is 50. Point 3 represents the midpoint of the loading cycle, with q at 100. Point 4 indicates the unloading period, where q is 50. Finally, Point 5 marks the completion of the loading period, with q returning to 0 for TL and TRL while for RL only point 1, 3 and 5 are relevant.

Fig. 5.14 is drawn after reaching the elastic state, and it is observed that once the elastic state is achieved, the isochrones drawn at the same time points consistently yield the same results. The isochrones are drawn for both Darcian and non-Darcian flow using the model parameters a=0.5, θ=0.5, and i_1=45. In the figures, the dotted line represents Darcian flow (DF), while the dashed line represents non-Darcian flow (NDF). Figs. 5.14a, 5.14b, and 5.14c illustrate the form of isochrones corresponding to R_T=∞, R_B=10 whereas, Figs. 5.14d, 5.14e, and 5.14f pertain to R_T=R_B=10. The figures are shown for all three chosen periodic loadings: (a) TL (Figs. 5.14a, 5.14d), (b) TRL (Figs. 5.14b, 5.14e), and (c) RL (Figs. 5.14c, 5.14f). Fig. 5.14a indicates that after the completion of the rest period (point 1), the pore water pressure (PWP) remains negative, suggesting that the negative PWP does not fully dissipate after unloading and resting time for all periodic loadings. The difference between the DF and NDF is greater for the first set boundary condition compared to the second. At point 2, for both TL and TRL, PWP is highest near the edges and smaller in the middle. The difference between DF and NDF is more pronounced in TL loading compared to TRL. At point 2, the rate of PWP dissipation is slower in DF than in NDF in the middle of the soil layer, while near the edges, the rate of dissipation is slower in NDF than in DF.

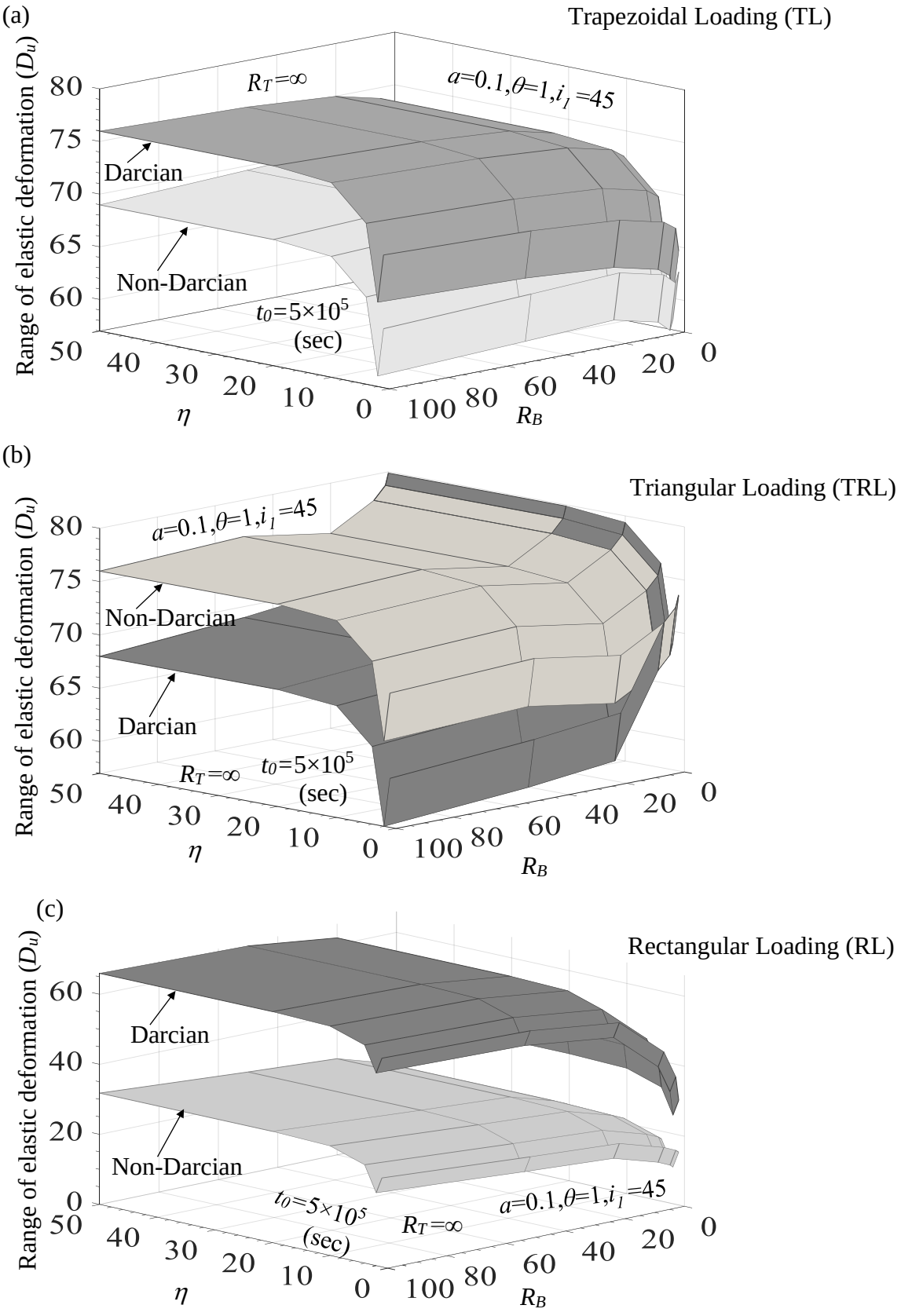

Fig 5.12 Combined impact of η and R_B on the range of elastic deformation (D_u) for Darcian and non-Darcian flow corresponding to: (a) TL, (b)TRL, and (c) RL.

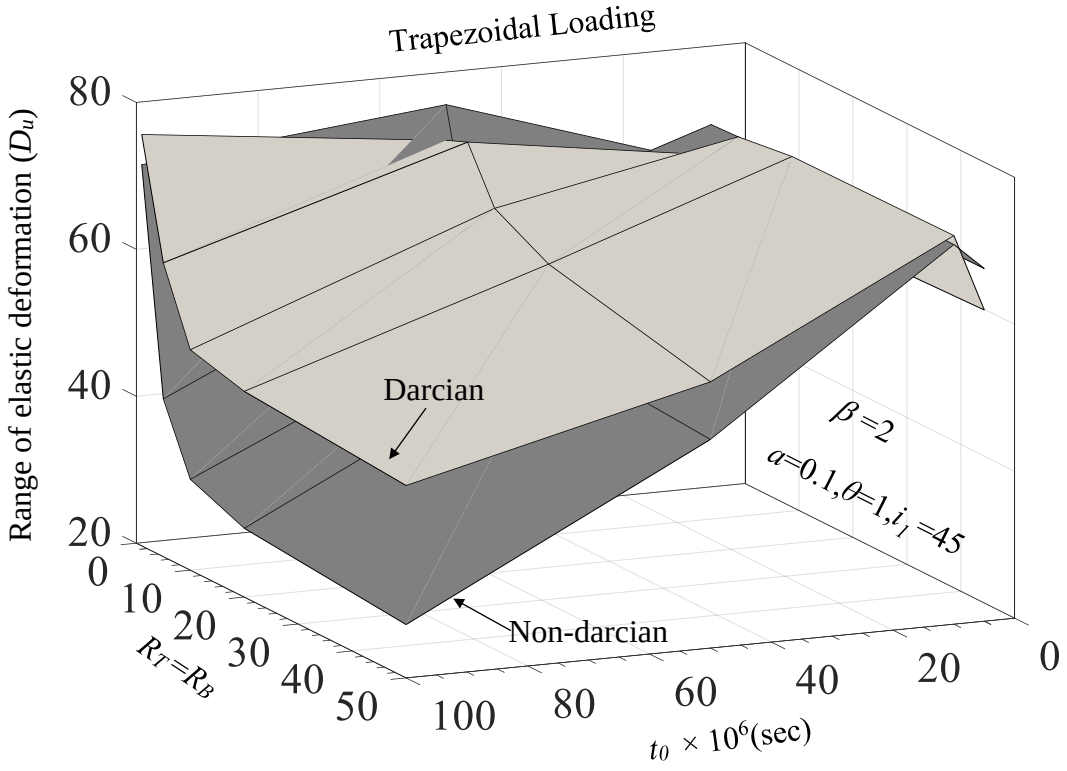

Fig 5.13 Combined impact of symmetric boundary condition and t_0 on range of elastic deformation (D_u) for Darcian and non-Darcian flow for the trapezoidal loading.

Point 3, which represents the middle of the loading period, shows that PWP is completely positive throughout the depth. Here, the rate of PWP dissipation for DF is equal to or slower than NDF in the middle, while near the edges, the rate of dissipation for DF is higher than NDF. At point 4, PWP is negative near the edges of the soil layer and positive in the middle. It can also be observed that the rate of PWP dissipation for NDF is less than for DF. Finally, point 5 shows that PWP is completely negative throughout the layer, with maximum negative PWP near the edges of the soil.

Fig. 5.15 shows the deformation isochrones for the cyclic loading at five different points.

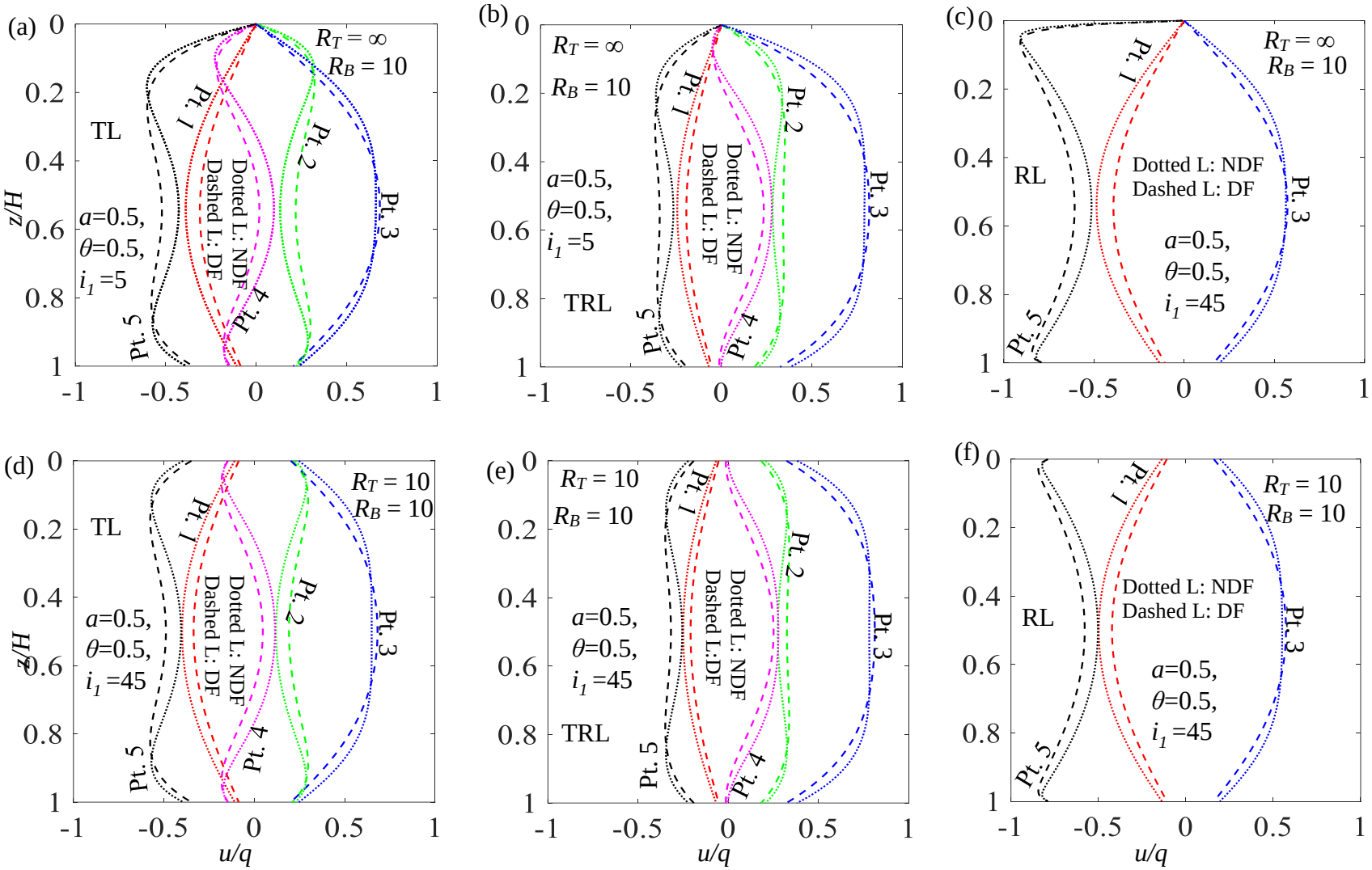

Fig 5.14 The variation of normalized isochrones at different loading positions of the (a,d) TL, (b,e) TRL, and (c,f) RL periodic loadings.

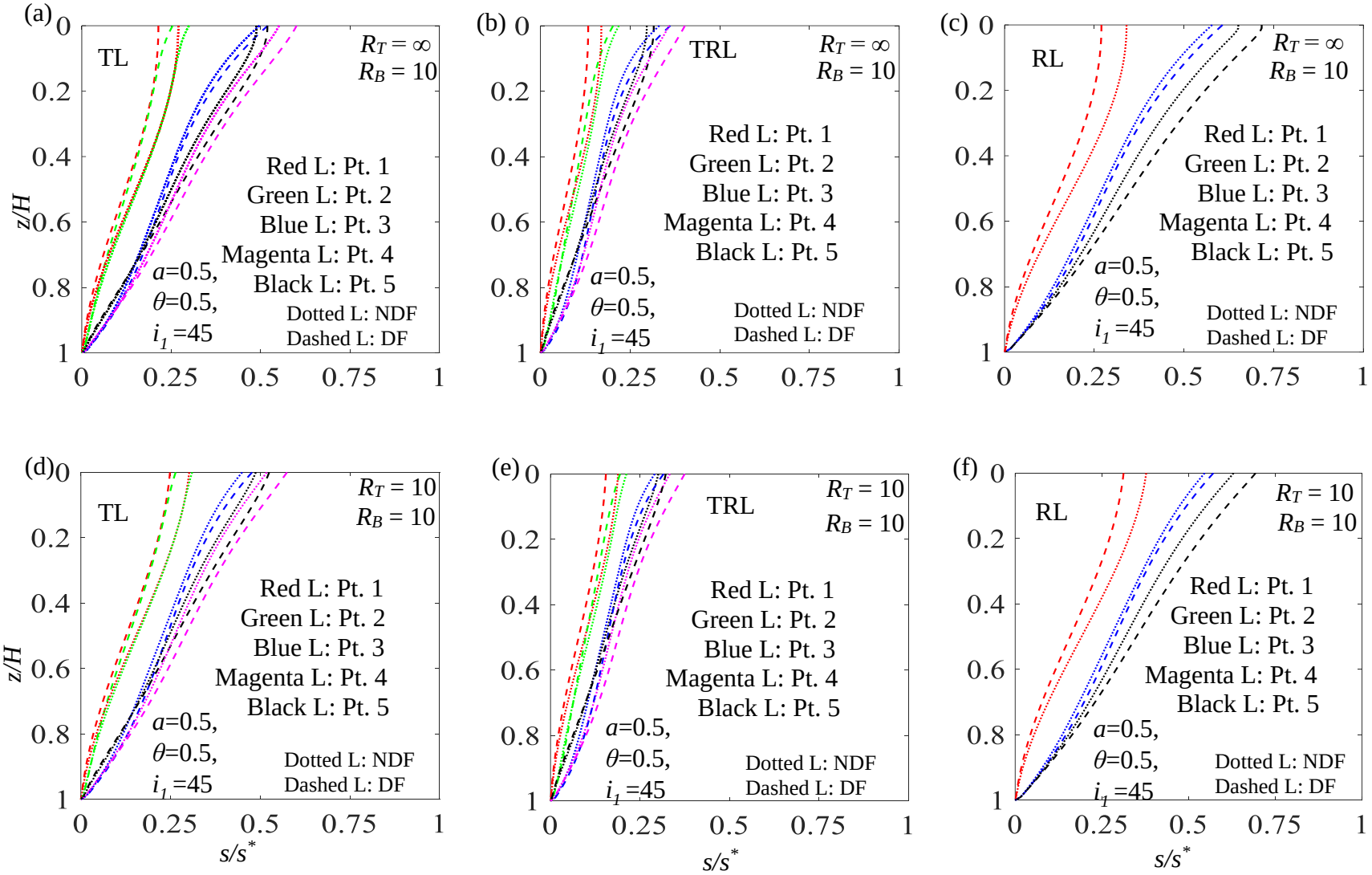

Fig 5.15 The variation of normalized settlement at different loading positions of the (a,d) TL, (b,e) TRL, and (c,f) RL periodic loadings.

The isochrones for both Darcian flow (DF) and non-Darcian flow (NDF) are drawn using the model parameters a=0.5, θ=0.5, and i_1=45. In the figures, the dashed line indicates Darcian flow (DF), while the dotted line indicates non-Darcian flow (NDF). Fig. 5.15a and 15d illustrate TL under two different sets of boundary conditions: (R_T=∞, R_B=10) and (R_T=R_B=10), respectively. Fig. 5.15b and 15e show TRL under the same two boundary conditions, and Fig. 5.15c and 15f depict RL under these same conditions. From Fig. 5.15 it can be observed that the deformation caused by Darcian flow (DF) is greater than that caused by non-Darcian flow (NDF). The minimum deformation occurs at point 1, while the maximum deformation is found at point 4 for TRL and TL, and at point 5 for RL.

5.5 SUMMARY

In this chapter, a rigorous numerical investigation is performed to assess the consolidation behavior of a homogeneous saturated clays bounded by semipermeable drainage surfaces and subjected to various forms of cyclic loadings. The fluid flow is considered to be governed by the exponential Elnagger et al.'s (1973) equation. The numerical simulations are performed with the aid of Crank-Nicolson semi-implicit finite difference scheme. By invoking the Biot's (1941) coupled equation, the pore water pressure and settlement both are evaluated simultaneously. By varying non-Darcian flow parameters, degree of drainage obstruction, loading period, no-load duration, a series of consolidation and settlement curves, PWP isochrones and settlement isochrones, PWP profiles are drawn. The analysis concludes that the boundary conditions, flow parameters, and loading type significantly impact the settlement and PWP variation.